



This is a repository copy of *Pulse propagation in turbidity currents*.

White Rose Research Online URL for this paper:  
<http://eprints.whiterose.ac.uk/150062/>

Version: Accepted Version

---

**Article:**

Ho, V.L., Dorrell, R.M., Keevil, G.M. et al. (2 more authors) (2018) Pulse propagation in turbidity currents. *Sedimentology*, 65 (2). pp. 620-637. ISSN 0037-0746

<https://doi.org/10.1111/sed.12397>

---

This is the peer reviewed version of the following article: Ho, V. L., Dorrell, R. M., Keevil, G. M., Burns, A. D. and McCaffrey, W. D. (2018), Pulse propagation in turbidity currents. *Sedimentology*, 65: 620-637., which has been published in final form at <https://doi.org/10.1111/sed.12397>. This article may be used for non-commercial purposes in accordance with Wiley Terms and Conditions for Use of Self-Archived Versions.

**Reuse**

Items deposited in White Rose Research Online are protected by copyright, with all rights reserved unless indicated otherwise. They may be downloaded and/or printed for private study, or other acts as permitted by national copyright laws. The publisher or other rights holders may allow further reproduction and re-use of the full text version. This is indicated by the licence information on the White Rose Research Online record for the item.

**Takedown**

If you consider content in White Rose Research Online to be in breach of UK law, please notify us by emailing [eprints@whiterose.ac.uk](mailto:eprints@whiterose.ac.uk) including the URL of the record and the reason for the withdrawal request.



[eprints@whiterose.ac.uk](mailto:eprints@whiterose.ac.uk)  
<https://eprints.whiterose.ac.uk/>

# 1 Pulse propagation in turbidity currents

2

3 Ho V. Luan<sup>1\*</sup>, Dorrell R.M.<sup>1</sup>, Keevil G.M.<sup>1</sup>, Burns A.D.<sup>2</sup> and McCaffrey W.D.<sup>1</sup>

4

5 1. School of Earth and Environment, University of Leeds, Leeds, LS2 9JT, UK.

6 2. School of Chemical and Process Engineering, University of Leeds, Leeds, LS2 9JT, UK.

7

8 \*Corresponding author: eevlh@leeds.ac.uk

9

## 10 **ABSTRACT**

11 Submarine turbidity currents are a key mechanism in the transportation of clastic sediments  
12 to deep seas. Such currents may initiate with a complex longitudinal flow structure comprising  
13 flow pulses (e.g. by being sourced from retrogressive sea floor slope failures) or acquire such  
14 structure during runout (e.g. following flow combination downstream of confluences). A key  
15 question is how far along channel pathway complex flow structure is preserved within  
16 turbidity currents as they run out and thus if flow initiation mechanism and proximity to  
17 source may be inferred from the vertical structure of their deposits. To address this question,  
18 physical modelling of saline flows has been conducted to investigate the dynamics of single-  
19 pulsed vs. multi-pulsed density driven currents. The data suggest that under most  
20 circumstances individual pulses within a multi-pulsed flow must merge. Therefore initiation  
21 signatures will only be preserved in deposits upstream of the merging point, and may be  
22 distorted approaching it; downstream of the merging point, all initiation signals will be lost.  
23 This new understanding of merging phenomenon within multi-pulsed gravity currents  
24 broadens our ability to interpret multi-pulsed turbidites.

25

26 **Keywords:** turbidity currents, multi-pulsed turbidity currents, seismo-turbidites, pulsed  
27 turbidites, stacked turbidites, signal shredding.

## 28 1. INTRODUCTION

29 Gravity currents are driven by a density difference between two fluids, and are widespread in  
30 both industrial scenarios and natural settings. Turbidity currents are a form of dilute  
31 particulate gravity flow in which the flows move under the gravitational action upon dispersed  
32 sediments suspended within the interstitial fluid (Middleton, 1993; Huppert, 1998; Kneller &  
33 Buckee, 2000; Sequeiros, 2012). Turbidity currents in natural settings can range up to  
34 hundreds of meter in thickness (Piper *et al.*, 1988; Sumner & Paull, 2014) with durations that  
35 may extend up to hours or days (Piper *et al.*, 1999; Xu *et al.*, 2004; Mikada *et al.*, 2006); they  
36 are a principal mechanism by which sediment is transported from continents to deep seas  
37 (e.g. Simpson, 1982; Talling *et al.*, 2015). Turbidity currents can be initiated by submarine  
38 slope failures (triggered by earthquakes or other mechanisms) or by direct hyperpycnal  
39 underflow into the oceans; they commonly flow through submarine channels into the deep  
40 oceans (Mulder & Alexander, 2001; Best, *et al.*, 2005; Piper & Normark, 2009).

41

42 Sediments deposited by turbidity currents – turbidites - commonly exhibit  
43 continuously upward fining of mean grain size (Fig. 1). This is referred to as “normal grading”  
44 (Bouma, 1962; Lowe, 1982; Gutiérrez-Pastor *et al.*, 2013). However, it is not uncommon for  
45 turbidites to show more complex grading profiles, such as inverse grading (e.g. Kneller and  
46 McCaffrey, 2003; Mulder *et al.*, 2003). On the basis that the grain size at any particular level  
47 in a deposit relates to the instantaneous basal shear stresses, normal grading suggests  
48 deposition from a waning flow, whereas, inversely graded (upward coarsening) deposits  
49 suggest deposition from waxing flow (Kneller & Branney, 1995; Kneller & McCaffrey, 2003;  
50 Mulder *et al.*, 2003; Amy *et al.*, 2005; Basilici *et al.*, 2012, cf. Hand, 1997). A more complex  
51 exception from normal grading patterns is seen when repeated intervals of coarsening are  
52 seen superimposed upon an overall normally-grading profile. Beds exhibiting this pattern are  
53 here described as a “pulsed” or “multi-pulsed” turbidites, as the implication is that pulses of  
54 increased velocity occurred in the overpassing flow at the point of deposition. Pulsed  
55 turbidites can be differentiated from “stacked” turbidites which, although superficially  
56 similar, represent the closely vertically juxtaposed deposits of two or more individual turbidity  
57 currents; in practice, distinguishing the two can be challenging where later flows erode into  
58 the deposits of earlier flows to produce deposit amalgamation and intervening fine grained

59 material is absent. When submarine turbidites show deviations from a continuous normal  
60 grading, a variety of mechanisms can be invoked to explain pulsed flow generation, for  
61 example discrete episodes of retrogressive slumping (Piper *et al.*, 1999; Canals *et al.*, 2004;  
62 Bull *et al.*, 2009), variations in ground shaking in currents initiated by single seismic events  
63 (Goldfinger *et al.*, 2012), variations in the flood hydrograph for hyperpycnally generated flows  
64 (Mulder & Alexander, 2001) and flow combination along the pathway of channel confluences  
65 (Nakajima & Kanai, 2000; Ismail, *et al.*, 2016). In addition flow reflection in confined settings  
66 has also been invoked to cause pulsing (e.g. Haughton, 1994). Research on how these  
67 mechanisms might be distinguished in the depositional record of pulsing flows is less  
68 extensive (see examples in Goldfinger *et al.*, 2012). A key consideration in this regard is how  
69 long non-monotonic variations in mean flow velocity along the flow may persist from source,  
70 and thus potentially be indicative of the flow generation mechanism; a related consideration  
71 is whether the degree to which a deposit approaches a normal grading profile may be an  
72 indirect indicator of distance from source.

73         Here, saline flow experiments are reported with the aim of informing understanding  
74 of the dynamics and evolution of pulsed turbidity currents, and exploring the possible  
75 implications for the interpretation of vertical depositional grading profiles. A principal goal is  
76 to review and extend the inferences regarding flow behaviour and proximity to source that  
77 can reasonably be made in natural turbidites. This contribution: i) presents novel  
78 experimental data that detail the variation of multi-pulsed flow dynamics; ii) assesses how  
79 flow dynamics may be interpreted from turbidite grading structure, and iii) reviews two case  
80 studies in the which the interpretational template of turbidites with complex grading profiles  
81 is reviewed and broadened.

## 82 **2. METHODOLOGY**

### 83 **2.1. Experimental set-up and research methodology**

84 The methodology of generating gravity currents in lock exchange flumes has been widely  
85 applied by various authors (e.g. Middleton, 1966; Holyer & Huppert, 1980; Britter & Simpson,  
86 1981; Lowe *et al.*, 2002; Gladstone *et al.*, 2004). In the work described here, lock exchange  
87 experiments of saline flows were conducted in order to gain an understanding of the internal  
88 dynamical structure of turbidity currents. Although they do not take into account the effects

89 of particle transport, as occurs in natural turbidity currents, saline flows are a well-established  
90 proxy for studying such flows (e.g. Kneller and Buckee, 2000; Islam and Imran, 2010; Hogg *et*  
91 *al.*, 2016). Similarly, turbulent laboratory-scale flows are thought to deliver a good  
92 representation of the dynamics of flow at natural scale (e.g. Paola *et al.*, 2009). Figure 2 shows  
93 the experimental set-up, in which a 5 m long Perspex flume with multiple lock-exchange gates  
94 was used, incorporating overspill boxes at both ends to reduce the effect of waves caused by  
95 the removal of the lock gates. Two 12.5 cm-long lock boxes were set up in series at one end  
96 to enable the generation of multi-pulsed flows, using saline fluid with 5% density excess ( $1050$   
97  $\text{kgm}^{-3}$ ) as a proxy for turbidity currents. Using a pneumatic lock-gate driver, the upstroke  
98 speed of each lock gate was set at  $1.0 \text{ ms}^{-1}$  so that any resulting turbulence was minimized,  
99 without being so slow that a partially-withdrawn lock gate affected the counter flow of fluid  
100 into the lock. The release time delay of the second gate could be adjusted to within  $1/10 \text{ s}$  of  
101 the first release; here it was set to  $4 \text{ s}$  so that the interaction between pulses in a bi-pulsed  
102 flow occurred within the length of the flume. To model single-pulsed flows, the delay was set  
103 to zero. The dense saline fluid was prepared in a 180 l mixer, and monitored to ensure  
104 consistent density. It was pumped slowly into the lock boxes via an intake valve on the bottom  
105 of each lock box, displacing fresh water above whilst preserving a sharp upper boundary. Each  
106 lock box was filled to a depth of  $0.05 \text{ m}$  with dense fluid dyed yellow in the first box and blue  
107 in the second to enhance flow visualization and front position tracking. The total lock box  
108 depth equalled the  $0.25 \text{ m}$  depth of the external ambient. The 1:5 depth ratio maintains fully  
109 turbulent, subcritical flow (Reynolds numbers were c. 2,000 and Froude numbers less than 1)  
110 while allowing suitable depth scaling approximating to real-world submarine flow, where flow  
111 to ambient depth ratios are 1:8 or greater (Piper *et al.*, 1988; Xu *et al.*, 2004).

112

113 Five HD interlinked cameras were deployed to capture a wide range of view of the  
114 flume. The cameras were carefully aligned so as to prevent image distortions and stitching  
115 artefacts. VirtualDub and Avisynth were used to stitch five linked video tracks together, based  
116 on an audio time cue; camera synchronization was within 1 frame ( $0.042 \text{ s}$ ). The alignment of  
117 the five cameras was checked using gridlines on the bottom of the flume (Fig. 3). The method  
118 of profiling Acoustic Doppler Velocimetry (ADV) was used to measure spatio-temporal  
119 variation of horizontal streamwise velocities (Craig *et al.*, 2011; MacVicar *et al.*, 2014; Brand

120 *et al.*, 2016). This methodology offers velocity profile measurements at high frequencies and  
121 with high resolution. The ADV probe head was positioned 7.1 cm above the bed of the flume  
122 at 13 different locations along the flume (Fig. 2), capturing a measurement of 30 mm flow  
123 depth at each position. Both the dense fluid and the ambient were seeded with neutrally-  
124 buoyant particles of 10  $\mu\text{m}$  diameter to generate a consistent acoustic reflection. Spatio-  
125 temporal depth-averaged velocity profiles were constructed for both single and multi-pulsed  
126 flows using the following equation:

$$127 \quad \bar{u} = \frac{\int_0^h v \, dz}{h}$$

128 where  $v$  is the instantaneous velocity of the flow and  $h = 0.03 \text{ m}$ .

## 129 **2.2. Dynamics of density currents**

130 The dynamics of lock-gate release density currents can usefully be associated with the  
131 slumping, inertial and viscous flow regimes of flow evolution, varying in each due to the  
132 changing relative significance of buoyancy, inertial and viscous forces (Huppert & Simpson,  
133 1980; Huppert, 1982; Rottman & Simpson, 1983; Bonnecaze *et al.*, 1993; Kneller *et al.*, 1999;  
134 Amy *et al.*, 2005; Di Federico *et al.*, 2006; Huppert, 2006; Sher & Woods, 2015). The slumping  
135 phase can extend up to 10 lock lengths from the initiation point; during this phase the gravity  
136 current is driven mainly by buoyancy forces resulting from the density difference between  
137 the dense fluid and the ambient. The buoyancy force of the flow is balanced by frictional  
138 forces, principally caused by the return flow of ambient fluid balancing the slumping of dense  
139 fluid out of the lock box; the flow travels with nearly constant velocity in the slumping phase.  
140 During the inertial phase, inertial effects become important; this regime is characterized by  
141 flow deceleration. Once the flow becomes sufficiently shallow, frictional forces exceed  
142 buoyancy and inertial forces, and the flow enters the viscous phase, in which it continues to  
143 decelerate.

144

## 145 **3. RESULTS**

146 Below, the results from the single- then multi-pulsed flows are described in sequence,  
147 considering firstly the flow visualization data and then the flow velocity data.

148

### 149 3.1 Single-pulsed flow

150 To distinguish the frontal and rearward components of the single-pulsed flow, the denser  
151 than ambient fluid in the front lock box was dyed yellow, and that in the rear blue, as shown  
152 in Fig. 3A. As noted above, a zero second delay time between two lock gates enabled the  
153 instantaneous trigger of the gates and the generation of a single release of the dense fluid.  
154 Following the release, the dense fluid in the lock boxes collapsed, forming a negatively  
155 buoyant density driven flow that propagated along the bottom of the flume. As the current  
156 advanced along the flume, the blue portion of dense fluid comprising the rear 50% of the flow  
157 at initiation was advected towards the front of the current (Fig. 3A,  $t=2-4$  s; cf. Sher & Woods,  
158 2015). The advection formed a visible intrusion around half of the flow depth, similar to  
159 advection in Poiseuille flow (Lowe *et al.*, 2002; Sher & Woods, 2015). The dyed components  
160 of the flow are inferred to have progressively mixed, changing the flow colour from  
161 yellow/blue to green. In addition, the variation in the degree of mixing between the dense  
162 fluid and the ambient is qualitatively indicated by the change in relative colour intensity of  
163 the green fluid (Fig. 3A,  $t=2-18$  s). This change is especially pronounced at the flow head,  
164 where turbulent mixing processes are largest, due to shear-driven generation of Kelvin-  
165 Helmholtz billows (Britter & Simpson, 1978; Johnson & Hogg, 2013).

166

167 The tracking of flow front positions using video data and the collection of velocity time  
168 series using fixed instrumentation at different downstream locations permit velocity profiles  
169 of both single- and multi-pulsed flows to be detailed (Figs. 4, 5 and 6). By tracking the positions  
170 of the front (yellow) and rear (blue) components of the single-pulsed flow, two dynamical  
171 flow regimes can be identified. In the initial slumping phase, the flow advanced at a nearly  
172 constant velocity of c.  $0.082 \text{ ms}^{-1}$  for 1.25 m (c. 5 lock lengths). During the succeeding inertial  
173 phase, the flow decelerated from  $0.082 \text{ ms}^{-1}$  to  $0.008 \text{ ms}^{-1}$  s over 2 m. The viscous phase of  
174 the flow was not observed in the length of the flume covered by the cameras. The rearward  
175 portion of the single-pulsed flow was advected forwards within the flow at a nearly constant  
176 velocity of  $0.1 \text{ ms}^{-1}$ , i.e., 25% faster than the flow head, reaching the flow front during the  
177 slumping phase some 0.8 m from source (Fig. 4A). The single-pulsed flow (Fig. 5A) displayed  
178 the rapidly waxing and progressively waning velocity structure which is usually observed in  
179 lock-gate release experiments (e.g. Simpson, 1982; Kneller *et al.*, 1999). The velocity

180 maximum was located at c. 25% of the local flow depth, as commonly seen in laboratory  
181 experiments, field data and theoretical models (e.g. Kneller & Buckee, 2000; Talling *et al.*,  
182 2015). The magnitude of flow velocity was observed to decrease with increasing time and  
183 distance from source, as indicated by the change in colour intensity in Fig. 5A. The depth of  
184 the flow may be estimated by using the vertical velocity profile to establish the height of the  
185 zero velocity contour that separates downstream from upstream (return) flow (Dorrell *et al.*,  
186 2016); e.g. in Fig. 5A at 0.365m downstream position and 2.5s,  $h=0.015\text{m}$ . The spatio-  
187 temporal variation of depth-averaged velocity for single-pulsed flow is shown in Fig. 6A in  
188 which the boundary of the black region indicates the arrival of the flow in time and space. The  
189 plot shows a model of standard flow evolution in which the head velocity, indicated by the  
190 yellow to orange regions behind the black edge, is constantly high within slumping phase (up  
191 to the distance of about 1.4 m in Fig. 6A) and then decreases with increasing time and  
192 distance.

193

### 194 **3.2. Multi-pulsed flow**

195 Initially, a single flow pulse dyed yellow was released from the front lock box and propagated  
196 along the flume in the form of a negatively-buoyant density current (Fig. 3B,  $t=2\text{ s}$ ). The second  
197 pulse was triggered 4 s after the first one, at which time the fluid comprising the initial release  
198 had collapsed to approximately one fourth of its initial depth in the front lock box (Fig. 3B,  $t=4$   
199 s). The second pulse was quickly advected towards the front of the flow, in the form of a  
200 visible intrusion with sharp boundaries, at approximately half of the height of the first pulse  
201 (Fig. 3B, inset  $t=11\text{ s}$ ). The colour change from yellow and blue to green reflects the  
202 progressive mixing between the two pulses (Fig 3B,  $t=11-18\text{ s}$ ). Eventually, the two pulses  
203 merged at a distance 1.4 m from source and the whole flow evolved in a manner similar to  
204 that of a single-pulsed flow during its inertial phase (Figs. 3 and 4). Kelvin-Helmholtz billows  
205 were generated on the back of the flow head, enhancing turbulent mixing in the flow and  
206 between the dense and ambient fluid (Britter & Simpson, 1978; Johnson & Hogg, 2013). Thus  
207 the colour shift at the flow head, as indicated by the variation in colour intensity of the green  
208 (mixed) fluid, was intensified (Fig. 3B,  $t=2-18\text{ s}$ ).

209 Front position tracking and the collection of velocity time series enabled velocity profiles of  
210 the multi-pulsed flows to be detailed (Figs. 5 and 6). The first pulse entered its slumping phase



211 at initiation, and had travelled at a nearly constant velocity of  $0.079 \text{ ms}^{-1}$  for 0.65 m,  
212 (approximately five 12.5 cm lock lengths) before the second pulse was released. The second  
213 pulse was released 4 s after the first (Figs. 4B and 5B) and progressively intruded into it. The  
214 combined flow accelerated at the point when the intrusion reached the flow head (Fig. 4B,  
215 inset) advancing at a nearly constant velocity of c.  $0.074 \text{ ms}^{-1}$  for 0.25 m from the point of  
216 merging. Thus, the slumping phase of the multi-pulsed flow lasted over 1.40 m (approximately  
217 six 25.0 cm lock lengths). The slumping phase ended at 1.65 m from source. The velocity of  
218 the second pulse averaged nearly  $0.110 \text{ ms}^{-1}$ , which is approximately 35% greater than the  
219 initial head velocity of the first pulse. The inertial phase of the merged multi-pulsed flow was  
220 characterized by a reduction in velocity to  $0.012 \text{ ms}^{-1}$  over a distance of about 1.85 m between  
221 1.65 m to 3.5 m from source (Fig. 4B). As with the single-pulsed flow experiments, the viscous  
222 phase of the multi-pulsed flow was not captured within the camera range of these  
223 experiments. The multi-pulsed flow displayed a more complex velocity structure than the  
224 generic waxing-waning velocity profile observed in lock-release single-pulsed gravity currents  
225 (Fig. 5B). Two separate pulses of relatively high velocity ( $>0.1 \text{ ms}^{-1}$ ) were distinctly observed  
226 proximally to source (Fig. 5B, 0.365 m). The time separation between two pulses decreased  
227 as the second pulse was progressively advected towards the front of the first pulse (e.g. Fig.  
228 5B, 0.365 m, 0.675 m and 0.865 m). At the point of merging, the two pulses tended to have  
229 similar velocities. Beyond the point of merging, the merged flow exhibited essentially the  
230 same waxing-waning velocity structure as observed in the single-pulsed flow experiments  
231 (Fig. 5A-B, 1.265 m, 1.665 m). The velocity maximum was also located at about 20% of the  
232 flow depth, as observed in the single-pulsed flow experiments. In order to visualize the spatio-  
233 temporal variation in the velocity profile of the multi-pulsed flow, a contour plot showing the  
234 depth-averaged velocity of the flow was constructed (Fig. 6B). The depth-averaged velocity  
235 of the first pulse was relatively high proximal to source ( $0.1 \text{ ms}^{-1}$ ). The high intensity region  
236 surrounding the dotted line on Fig. 6B indicates the signal of the advection of the second pulse  
237 within the first pulse. The initial relative timing of this signal was distorted by being  
238 progressively reduced towards the point of merging. Beyond this point, the signal of the  
239 second pulse intrusion in the velocity profile was completely lost (i.e., “shredded”, *sensu*  
240 Jerolmack & Paola, 2010; Figs. 5B and 6B).

241

### 242 **3.3. Single-pulsed vs. multi-pulsed flows**

243 Multi-pulsed flow evolution is characterized by interaction of the separate pulses which  
244 eventually merge at some distance from source; such flows exhibit a pulsing character up to  
245 the point of merging. This pulsing characteristic is not seen in single-pulsed density currents.  
246 Figure 7A shows raw (unfiltered) data detailing the temporal variation of depth-averaged  
247 velocities of the single- vs. multi-pulsed flows, shown proximally to source, at the point of  
248 merging and distally from source. The surface waves set up at flow initiation were not  
249 completely removed by the overspill boxes, and resulted in a fluctuation in the raw data; the  
250 magnitudes of the fluctuations are relatively small compared to the front velocity of the flows,  
251 and are not thought to have significantly influenced the flow dynamics. To more clearly assess  
252 the flow dynamics, the raw velocity data are filtered and replotted in Fig. 7B. Before the point  
253 of merging, the depth averaged velocity profile of single-pulsed flows exhibited a standard  
254 waxing-waning velocity structure whereas the profile of multi-pulsed flows has two  
255 pronounced pulses (0-7 s at 0.365 m Fig. 7B). The time delay measured between the two  
256 velocity pulses depends on initial lag time at initiation, and also upon the point of  
257 measurement. Up to the point of merging, the time separation between the two pulses in  
258 multi-pulsed flows progressively decreased. For the multi-pulsed flow, after the peak of the  
259 second pulse passed the position of profiling, the velocity magnitude of the flow became  
260 comparable to that of a single-pulsed flow comprising the same initial dense fluid. In distal  
261 regions, both single- and multi-pulsed flows showed similar velocity structures to the normal  
262 waxing-waning velocity profile (Fig. 7B).

263

## 264 **4. DISCUSSION**

### 265 **4.1. Multi-pulsed turbidity current propagation**

266 Turbidity currents commonly develop vertical density stratification during runout, due to the  
267 entrainment of ambient fluid (Britter & Simpson, 1978; Hallworth *et al.*, 1996), particle  
268 settlement (Baas *et al.*, 2005) and also due to recirculation of fluid from the body into the  
269 head, where it is mixed and ejected backwards (Lowe *et al.*, 2002; Sher & Woods, 2015;  
270 Hughes, 2016). It is inferred that both the single-pulsed density currents and the first pulse of  
271 multi-pulsed flows developed vertical density stratification; the change within the first pulse

272 from an initial vertically homogeneous density profile to a stratified one can be seen from the  
273 development of a green to yellow vertical transition in the single-pulsed flow (Fig. 3A) and in  
274 the upward-lightening yellow colour intensity in the multi-pulsed flow (Fig. 3B). Consequently  
275 the second pulse intruded into the first at a neutrally buoyant level and was advected within  
276 it.

277 In gravity currents the velocity maximum is usually at approximately one quarter of  
278 the flow depth, with the maximum velocity being greater than the speed of the flow front  
279 (Figs. 3 and 5, Kneller *et al.*, 1999; Lowe *et al.*, 2002; Sher & Woods, 2015). Consequently,  
280 material from the back of the flow is advected towards the head (e.g. Sher & Woods, 2015);  
281 Gladstone *et al.*, (2004) noted in this regard that density stratification in the pre-release fluid  
282 leads to preferential advection of lighter fluid towards the flow front. However, previous  
283 studies have focused on the case in which flow properties vary monotonically behind the  
284 head, and not considered the case in which the longitudinal velocity structure is  
285 heterogeneous, i.e., when multiple pulses are initiated separately in time but eventually  
286 merge distally from source, resulting in cyclic waxing-waning velocity structure in the flow  
287 dynamics.

288 Here advection is visualized by separating both single- and multi-pulsed flows into  
289 primary and secondary components, corresponding to the front and back of the flow at  
290 initiation (Fig. 3). In the single-pulsed flow, the second component essentially moved with the  
291 fluid immediately in front, and quicker than the current head velocity. In the multi-pulse  
292 flows, the internal fluid velocity of the second pulse exceeded both that of the fluid pulse  
293 immediately preceding it and of the current head velocity (Fig. 6 and section 4.2), resulting in  
294 the forward advection of the second pulse being accelerated compared to that of the second  
295 flow component in the single-pulsed flows. The tracked advection rates of the second pulse  
296 in multi-pulsed flows were 10% larger than the internal flow front visualized in the single-  
297 pulsed flows, i.e., c  $0.11 \text{ ms}^{-1}$  vs.  $0.10 \text{ ms}^{-1}$  (Fig. 4). The increase in internal advection may in  
298 part be attributed to the additional momentum generated by the second lock-gate release.  
299 Effectively, in multi-pulse system the second flow component is restrained by the second lock  
300 gate, against gravity, for longer than in the single-pulse experiments. Thus, the delay between  
301 two releases creates a greater pressure difference in the multi-pulse system than that in the  
302 single-pulse system, due to the difference in the height of dense fluid in the two lock boxes.

303 By the time of the second lock gate release, the enhanced pressure gradient results in the  
304 formation of an internal wave and thus an increase in internal advection rates in the multi-  
305 pulse system.

306 Furthermore, in the multi-pulse system, the second pulse is released into the stratified  
307 remnant of the primary pulse. Stratification of the primary pulse is driven by entrainment of  
308 ambient fluid into the primary pulse after it has been released. The secondary pulse therefore  
309 forms and propagates on a neutrally buoyant level, in a similar fashion to intrusions in  
310 stratified quiescent fluids (Britter & Simpson, 1981; de Rooij *et al.*, 1999; Bolster *et al.*, 2008)  
311 but here modulated by the background velocity field of the primary pulse. As mixing induced  
312 stratification gradually decreases density of the primary pulse towards the density of the  
313 ambient, and as the secondary pulse is denser than the ambient, the secondary pulse will be  
314 confined within the primary pulse. If the secondary pulse is denser than the primary pulse the  
315 intrusion will occur along the lower boundary of the flow. A consequence is that the second  
316 pulse will experience reduced drag as its interaction with the solid lower and upper flow-  
317 ambient fluid boundary is limited, i.e. lower and upper interface shear-stress (Härtel *et al.*,  
318 2000) is reduced in comparison to single, or the primary component of multi-pulse flows (Fig.  
319 8).

320 Given that internal fluid velocity in the body of a gravity current is always greater than  
321 the head velocity (Kneller *et al.*, 1999; Lowe *et al.*, 2002; Sher & Woods, 2015), once a  
322 following pulse has begun to interact with the velocity field of the first pulse, the second pulse  
323 must eventually be advected towards the flow front. Therefore, it is concluded that the  
324 intrusion of the second pulse and the merging of two pulses seen in the experiments is an  
325 inevitable consequence of the interaction between pulses within dilute multi-pulsed density  
326 flows.

327

#### 328 **4.2. Conceptual models of deposition from multi-pulsed flows**

329 Since the flow dynamics of multi-pulsed flows vary along the flow pathway differently to those  
330 of single-pulsed flows, the spatial evolution of their deposits is expected to be distinguishable.  
331 Given that upward-fining and upward-coarsening grading patterns suggest deposition from

332 waning and waxing turbidity currents, respectively (Kneller & Branney, 1995; Hand, 1997;  
333 Mulder *et al.*, 2003; Amy *et al.*, 2005; Basilici *et al.*, 2012), the waxing-waning phenomenon  
334 within multi-pulsed flows should lead to the deposition of inverse graded intervals  
335 corresponding the passage of a pulse (assuming the flow remains depositional and that an  
336 appropriate range of grain sizes is available for transport). In addition, the grading patterns of  
337 multi-pulse turbidites likely vary from proximal to distal regions, due to the progressive  
338 advection of pulses towards the flow front with increasing run-out distance. This advection  
339 should result in a progressive reduction in the time between pulses, decreasing to zero at the  
340 point of merging with the flow head; where multiple pulses are present, some may  
341 amalgamate before this point. Hence, in any associated turbidite deposit, an original pulsing  
342 signal might be relatively accurately preserved proximally, such that the relative spacing  
343 between inverse to normal grading cycles is representative of the timing differences between  
344 pulses at initiation. The signal might then be progressively distorted up to the point of  
345 merging, expressed in reductions in the relative vertical spacing of inverse to normal grading  
346 cycles and also in a reduction in the number of such cycles present. The signal will eventually  
347 be lost once all pulse components of the flow have completely merged. It should be noted  
348 that the relative spacing between cycles will also be dependent on the sedimentation rate.

349         Figure 9 shows the likely links between a range of turbidity current types, as defined  
350 by their longitudinal velocity structures, and their associated turbidite deposits. The deposits  
351 are based upon usage in, e.g. Bouma (1962), Lowe (1982) and Gutiérrez-Pastor *et al.*, (2013)  
352 and references therein. Thus single turbidites with normal grading are deposited by single-  
353 pulsed turbidity currents (Fig. 9A). Stacked turbidites represent the closed vertically  
354 juxtaposed deposits of two or more such flows (Fig. 9B); the close spacing is taken to imply  
355 short inter-flow time durations. Amalgamated turbidites (Fig. 9C) are compound deposits of  
356 two (or more) flows in which the later flow eroded into the deposits of the earlier flows.  
357 Pulsed turbidites (Fig. 9D) are the deposits of multi-pulsed flows whose individual pulses have  
358 interacted; depending on the cause of the pulsing, during early pulse interaction (e.g. Fig. 9D-  
359 i) each deposition interval may be similar to a single turbidite, but without any evidence that  
360 might indicate a period of flow inactivity between each one (e.g. turbidite mud or  
361 hemipelagite). When the pulses have significantly interacted (e.g. Fig. 9D-ii) the time  
362 separation between them, and thus the vertical separation of cycles in the deposit, will be

363 reduced. Note: the terms pulsed and stacked turbidites are used here regardless of the  
364 originating mechanism of the pulses or whether pulses have distinct mineralogical character.

365 The initial delay times between different pulses in a multi-pulsed flow depend on the flow  
366 generation mechanisms. For a flow initiated by a series of retrogressive submarine landslides,  
367 each pulse can be linked to a discrete slumping episode and thus the delay times between  
368 individual pulses are controlled by the timing between successive failures. This timing may  
369 relate to the natural rate of slope instability propagation, but for a flow initiated by a single  
370 large multi-pulsed earthquake or by closely spaced initial shocks and aftershocks (e.g.  
371 Goldfinger *et al.*, 2012), the delay times may relate to the spacing between different  
372 components of the seismic shock. When a multi-pulsed flow is formed by the combination at  
373 channel confluences of different single-pulsed turbidity flows, which were initially triggered  
374 synchronously in different channel heads, the delay time between pulses depends on the  
375 arrival time differences of the individual flows at the confluence (which depend in turn on  
376 channel lengths and intra channel flow velocities). The implications for deposit interpretation  
377 for each of these formation mechanisms are considered below.

378         The depositional structure of flows initiated by retrogressive slope failures (whether  
379 seismically generated or not) is shown in Fig. 10A. If there is no initial interaction between the  
380 two single-pulsed flows, stacked turbidites could be expected to form proximally. If the flows  
381 start to interact, the second flow would behave as a second pulse in a combined flow, and  
382 would thus be advected progressively towards the front of that flow. The vertical depositional  
383 structure would transition along the flow pathway from having a stacked to multi-pulsed  
384 character, finally becoming uni-pulsed (or single-pulsed) after the point of pulse merging.  
385 When initially distinct flows combine at confluences, the longitudinal variation in the vertical  
386 grading structure of associated turbidites is expected to be similar to that postulated in Fig.  
387 10A, but with an additional pulsing character acquired at the point of combination. In Fig. 10B  
388 a case is shown in which flows are triggered synchronously in each of three channels C1, C2  
389 and C3 but take different times to reach their first downstream confluence. This 3D model is  
390 extrapolated from the 2D experimental configuration. The actual deposit character will vary  
391 depending on the magnitude of each pulse and the nature of the setting. For example, a bi-  
392 pulsed flow is shown forming at the C1-C2 confluence, and persisting to from C1-C2 to C3  
393 confluence, where it merges with the flow in C3 to make a tri-pulsed flow that eventually

394 evolves into a uni-pulsed flow. However, had the constituent pulses of the flow formed at the  
395 C1-C2 confluence already merged before the C1-C2 to C3 confluence, uni-pulsed flows in  
396 channels C1-C2 and C3 would have combined to make a bi-pulsed flow, depositing a bi-pulsed  
397 turbidite immediately downstream, and a uni-pulsed turbidite more distally. If the delay times  
398 between flows were sufficiently long to prevent their interaction single turbidites would be  
399 deposited in each of channels C1, C2 and C3, two stacked turbidites would be deposited  
400 downstream of the C1-C2 confluence and three downstream of the C1-C2 to C3 confluence.  
401 In complex natural settings, multi-pulsed turbidity currents can be generated by both  
402 retrogressive slumping, with pulse timing either dictated by the timing of seismic shaking or  
403 by unforced slope failure processes, and by flow combination at confluences of flows that  
404 may or may not have a primary pulsed character.

405 It should be noted that the depositional models proposed in Fig. 10 disregard the  
406 effects of flow bypassing (e.g. Stevenson *et al.*, 2013; Talling, 2013) or erosion and of local  
407 topography features (Eggenhuisen *et al.*, 2010). Were bypassing or erosion to occur during  
408 flow run-out, some parts of the vertical grading profiles described in the figure might be  
409 partially or fully absent, with concomitant increases in deposit thicknesses further  
410 downstream.

411

### 412 **4.3. Seismo-turbidites**

413 Earthquake-triggered turbidites are commonly deposited along large, active tectonic margins  
414 such as Cascadia and Sumatra (Goldfiner *et al.*, 2007; St-Onge *et al.*, 2012). The deposits of  
415 flows generated in this way are called “seismo-turbidites” (*sensu* Shiki *et al.*, 2000, and  
416 references therein). Here the potential application of the conceptual models described above  
417 is investigated, both to refine models of flow evolution and to suggest new interpretational  
418 options. Sumner *et al.* (2013) document drop-core – derived records of Holocene turbidites  
419 deposited on the southwest Sumatra margin, and consider whether they were seismically  
420 triggered. Of interest here are turbidites with complex grading patterns, such as those  
421 recovered from the updip 4MC and downdip 2MC locations (Fig. 11A). At the 4MC location a  
422 succession of three turbidite units without intervening hemiplegic sediments have a  
423 deposition motif that could be interpreted either as stacked turbidites (separate events, Fig.

424 9B), the interpretation favoured by Sumner *et al.* (2013), or as a tri-pulsed turbidite (one  
425 event, Fig. 9D), deposited by a single, pulsed, seismically-generated turbidity current. The  
426 sequence of deposits at 2MC appears to comprise one thick basal turbidite and two much  
427 thinner overlying turbidites (Sumner *et al.*, 2013); the overall upward-fining grading profile of  
428 the basal 2MC turbidite suggests that it is the deposit of a single-pulse flow (e.g. Fig. 10A).  
429 Sumner *et al.*, (2013) did not correlate the 2MC deposit to other turbidites found locally in  
430 the system such as those at 4MC. Although this interpretation may correctly reflect that the  
431 4MC and 2MC locations did not lie on the same fairway, an alternative explanation now  
432 permitted by the work detailed here is that the 4MC tri-pulsed turbidite and the uni-pulsed  
433 2MC turbidite could represent the deposits of a single flow that was tri-pulsed at 4MC but  
434 evolved via pulse merging to be uni-pulsed at 2MC (Fig. 10). In this interpretation, the pattern  
435 of ground shaking that initiated flow might be distinguishable in the deposits at 4MC, but  
436 have been shredded at 2MC.

437 Cascadia channel is the channel that extends downstream from the confluence of the  
438 Juan de Fuca and Willapa channels (Fig. 11B; Goldfinger *et al.*, 2016). Core-based studies of  
439 Holocene sediments suggest that great earthquake shocks/aftershocks commonly result in  
440 the deposition of multi-pulsed turbidites in the Cascadia Basin (Goldfinger *et al.*, 2007;  
441 Gutiérrez-Pastor *et al.*, 2013). For example, where the same number of turbidites are found  
442 in each of the tributary channels and downstream of confluence of a linked channel system,  
443 it can be inferred that seismic events synchronously triggered turbidity currents in each of the  
444 tributaries, such that turbidity currents combined at confluences (Goldfinger *et al.*, 2012).  
445 Thus, should the number of coarse-grained sediment intervals within a correlated bed  
446 increase downstream of a confluence, the extra pulses were likely generated by a flow  
447 combination mechanism similar to that outlined in Fig. 10B. Figure 11B provides an example  
448 of such an increase, in which the “T3” bi-pulsed turbidite found at the 12PC location in the  
449 upstream Juan de Fuca channel is correlated with a tri-pulsed T3 at the 25PC location in the  
450 downstream Cascadia channel. The thickest interval of coarse sediments at 25PC is attributed  
451 to a single pulse flow component derived from the Willapa channel that mixed with a bi-  
452 pulsed flow from the Juan de Fuca channel (Fig. 11B; Gutiérrez-Pastor *et al.*, (2013).  
453 Gutiérrez-Pastor *et al.*, (2013), Goldfinger *et al.*, (2008), Goldfinger *et al.*, (2012) and Patton  
454 *et al.*, (2015) recognize that the pattern of pulsing seen in the majority of Holocene and late



455 Pleistocene turbidites correlated along the Cascadia margin appears to be consistent within  
456 each deposit. They interpret the multi-pulsed character of these beds to indicate flow  
457 initiation by the large magnitude ( $M > 9$ ) seismic events that characterize this margin. In this  
458 interpretation the apparent spatial persistence of pulsing character is contrary to the  
459 expectation of pulse merging described above. Either the pulses arise another way, the pulse  
460 merging phenomenon observed at laboratory scale does not occur within larger scale  
461 turbidity currents, or the merging length scale in such natural settings is longer than the  
462 spacing of sample locations. Further work is required to assess these possible explanations.

463

## 464 5. CONCLUSIONS

465 Physical modelling of multi-pulsed, solute density flows suggest that under most  
466 circumstances individual pulses within such flows must be advected forwards through the  
467 flow until they merge with the flow head. In natural dilute particulate gravity currents  
468 (turbidity currents), such pulsing flow structure may be acquired at flow initiation and be  
469 represented in any deposits by an interval of inverse grading (i.e., upwards coarsening) for  
470 each pulse. Assuming that such pulses are progressively advected towards the flow front with  
471 natural turbidity currents, a progressive reduction in the time between pulses is expected in  
472 progressively more distal locations, eventually decreasing to zero when the pulse merges with  
473 the flow head. Therefore an original pulsing signal might be relatively accurately preserved  
474 proximally, become progressively distorted up to the point of merging where the signal is  
475 completely lost ("signal shredded"). This may explain why normal grading is the predominant  
476 turbidite grading style in distal locations. Pulsing flow character may also arise when  
477 synchronously triggered flows combine at confluences; forward pulse advection will also  
478 progressively distort then shred pulses of this character. In natural settings, such as the  
479 Cascadia margin, the development of flow pulsing has already been inferred from the grading  
480 patterns within turbidites deposited downstream of confluences. The possibility that multi-  
481 pulsed flows may evolve spatially to become uni-pulsed can be invoked in studies of turbidites  
482 deposited on the southwest Sumatra margin, and permits a wider range of potential  
483 correlations to be considered. The multi-pulsed saline flows presented in this paper show  
484 that pulse merging is effectively inevitable whilst interacting primary and secondary pulses  
485 remain active. Given that waning flows suggest upward fining deposition and waxing flows

486 suggest the opposite, the extrapolation to predict the depositional patterns of pulsed  
487 turbidites appears reasonable. Nevertheless, the extrapolation should ideally be supported  
488 by experimental models of sediment-bearing flows together with a scaling analysis to more  
489 robustly link the characteristic lengths of pulse merging at laboratory scale and those at  
490 natural system scale; both are the subject of ongoing work.

491

## 492 **ACKNOWLEDGEMENTS**

493 This study was funded by Turbidites Research Group (sponsors: Anadarko, BG, BP,  
494 ConocoPhillips, Dana, ENI, Nexen, OMV, Petronas, Shell, Statoil, Tullow, Woodside). All  
495 authors have no conflict of interest to declare. We would like to thank Robert Thomas and  
496 Helena Brown in the Sorby Environmental Fluid Dynamics Laboratory, University of Leeds for  
497 their assistance with the experiments. We would also like to thank Associate Editor J. Baas,  
498 reviewers C. Goldfinger, S. Southern and an anonymous reviewer for their constructive  
499 comments on an earlier version of this paper.

500

## 501 **REFERENCES**

502 **Amy, L. A., Talling, P. J., Peakall, J., Wynn, R. B. and Arzola Thynne, R. G.** (2005) Bed geometry  
503 used to test recognition criteria of turbidites and (sandy) debrites. *Sed. Geol.*, **179**, 163–  
504 174.

505 **Baas, J. H., Houghton, P. D. W. and Choux, C.** (2005) Coupling between suspended sediment  
506 distribution and turbulence structure in a laboratory turbidity current. *J. Geophys. Res.*,  
507 **110**, doi:10.1029/2004JC002668.

508 **Basilici, G., de Luca, P. H. V. and Poiré, D. G.** (2012) Hummocky cross-stratification-like  
509 structures and combined-flow ripples in the Punta Negra Formation (Lower-Middle  
510 Devonian, Argentine Precordillera): A turbiditic deep-water or storm-dominated  
511 prodelta inner-shelf system? *Sed. Geol.*, **267–268**, 73–92.

- 512 **Best, J. L., Kostaschuk, R. A., Peakall, J., Villard, P. V. and Franklin, M.** (2005) Whole flow field  
513 dynamics and velocity pulsing within natural sediment-laden underflows. *Geology*,  
514 **33(10)**, 765–768.
- 515 **Bonnecaze, R. T., Huppert, H. E. and Lister, J. R.** (1993) Particle-driven gravity currents. *J. Fluid*  
516 *Mech.*, **250**, 339–369.
- 517 **Bolster, D., Hang, A. and Linden, P. F.** (2008) The front speed of intrusion into a continuously  
518 stratified medium. *J. Fluid Mech.*, **594**, 369–377.
- 519 **Bouma, A.H.** (1962) Sedimentology of some Flysch Deposits: A Graphic Approach to Facies  
520 Interpretation. Elsevier, Amsterdam, 168 pp.
- 521 **Brand, A., Noss, C., Dinkel, C. and Holzner, M.** (2016) High-resolution measurements of  
522 turbulent flow close to the sediment-water interface using a bistatic acoustic profiler.  
523 *Journal of Atmospheric and Oceanic Technology*, **33**, 769–788.
- 524 **Britter, R. E. and Simpson, J. E.** (1978) Experiments on the dynamics of a gravity current head.  
525 *J. Fluid Mech.*, **88**, 223–240.
- 526 **Britter, R. E. and Simpson, J. E.** (1981) A note on the structure of the head of an intrusive  
527 gravity current. *J. Fluid Mech.*, **112**, 459–466.
- 528 **Bull, S., Cartwright, J. and Huuse, M.** (2009) A subsurface evacuation model for submarine  
529 slope failure. *Basin Res.*, **21**, 433–443.
- 530 **Canals, M., Lastras, G., Urgeles, R., Casamor, J. L., Mienert, J., Cattaneo, A., De Batist, M.,**  
531 **Haflidason, H., Imbo, Y., Laberg, J. S., Locat, J., Long, D., Longva, O., Masson, D. G.,**  
532 **Sultan, N., Trincardi, F. and Bryn, P.** (2004) Slope failure dynamics and impacts from  
533 seafloor and shallow sub-seafloor geophysical data: Case studies from the COSTA  
534 project. *Mar. Geol.*, **213**, 9–72.
- 535 **Craig, R. G. A., Loadman, C., Clement, B., Rusello, P. J. and Siegel, E.** (2011) Characterization  
536 and testing of a new bistatic profiling acoustic doppler velocimeter: The Vectrino-II.

- 537 Proceedings of the IEEE/OES/CWTM *Tenth Working Conference on Current*  
538 *Measurement Technology*, Monterey, CA, 246–252.
- 539 **de Rooij, F., Linden, P. F. and Dalziel, S. B.** (1999) Saline and particle-driven interfacial  
540 intrusions. *J. Fluid Mech.*, **389**, 303-334.
- 541 **Di Federico, V., Cintoli, S. and Bizzarri, G.** (2006) Viscous spreading of non-Newtonian gravity  
542 currents in radial geometry. *WIT Transactions on Engineering Sciences*, **52**, 399–408.
- 543 **Dorrell, R. M., Peakall, J., Sumner, E. J., Parsons, D. R., Darby, S. E., Wynn, R. B., Özsoy, E.**  
544 **and Tezcan, D.** (2016) Flow dynamics and mixing processes in hydraulic jump arrays:  
545 Implications for channel-lobe transition zones. *Mar. Geol.*, **381**, 181–193.
- 546 **Eggenhuisen, J. T., McCaffrey, W. D., Haughton, P. D. W. and Butler, R. W. H.** (2010) Small-  
547 scale spatial variability in turbidity-current flow controlled by roughness resulting from  
548 substrate erosion: field evidence for a feedback mechanism. *J. Sed. Res.*, **80**, 129-136.
- 549 **GebCO** (2014) [http://www.gebco.net/data\\_and\\_products/gridded\\_bathymetry\\_data/](http://www.gebco.net/data_and_products/gridded_bathymetry_data/)
- 550 **Gladstone, C., Ritchie, L. J., Sparks, R. S. J. and Woods, A. W.** (2004) An experimental  
551 investigation of density-stratified inertial gravity currents. *Sedimentology*, **51**, 767-789.
- 552 **Goldfinger, C., Galer, S., Beeson, J., Hamilton, T., Black, B., Romsos, C., Patton, J., Nelson C.**  
553 **H., Hausmann, R. and Morey, A.** (2016) The importance of site selection, sediment  
554 supply, and hydrodynamics: A case study of submarine paleoseismology on the northern  
555 Cascadia margin, Washington USA. *Mar. Sed.*, (2016).  
556 <https://doi.org/10.1016/j.margeo.2016.06.008>
- 557 **Goldfinger, C., Grijalva, K., Bürgmann, R., Morey, A.E., Johnson, J.E., Nelson, C.H., Gutiérrez-**  
558 **Pastor, J., Ericsson, A., Karabanov, E., Chaytor, J.D., Patton, J. and Gràcia, E.** (2008) Late  
559 Holocene rupture of the northern San Andreas fault and possible stress linkage to the  
560 Cascadia subduction zone. *Earth Bulletin of the Seismological Society of America*, **98(2)**,  
561 861–889.

- 562 **Goldfinger, C., Morey, A. E., Nelson, C. H., Gutiérrez-Pastor, J., Johnson, J. E., Karabanov, E.,**  
563 **Chaytor, J. and Eriksson, A.** (2007) Rupture lengths and temporal history of significant  
564 earthquakes on the offshore and north coast segments of the Northern San Andreas  
565 Fault based on turbidite stratigraphy. *Earth Planet. Sci. Lett.*, **254**, 9–27.
- 566 **Goldfinger, C., Nelson, C.H., Morey, A.E., Johnson, J.E., Patton, J., Karabanov, E., Gutiérrez-**  
567 **Pastor, J., Eriksson, A.T., Gràcia, E., Dunhill, G., Enkin, R.J., Dallimore, A. and Vallier, T.**  
568 (2012) Turbidite event history—methods and implications for Holocene paleoseismicity  
569 of the Cascadia subduction zone. U.S. Geological Survey Professional Paper 1661-F, 170p.  
570 (Available free at <http://pubs.usgs.gov/pp/pp1661f/>).
- 571 **Gutiérrez-Pastor, J., Nelson, C. H., Goldfinger, C. and Escutia, C.** (2013) Sedimentology of  
572 seismo-turbidites off the Cascadia and northern California active tectonic continental  
573 margins, northwest Pacific Ocean. *Mar. Geol.*, **336**, 99–119.
- 574 **Hallworth, M. A., Huppert, H. E., Phillips, J. C. and Sparks, R. S. J.** (1996) Entrainment into  
575 two-dimensional and axisymmetric turbulent gravity currents. *J. Fluid Mech.*, **308**, 289–311.
- 576 **Hand, B. M.** (1997) Inverse grading resulting from coarse-sediment transport lag. *J. Sed. Res.*,  
577 **67(1)**, 124-129.
- 578 **Härtel, C., Meiburg, E. and Necker, F.** (2000) Analysis and direct numerical simulation of the  
579 flow at a gravity current head. Part 1. Flow topology and front speed for slip and no-slip  
580 boundaries. *J. Fluid Mech.*, **418**, 189–212.
- 581 **Haughton, P. D. W.** (1994) Deposits of deflected and ponded turbidity currents, Sorbas Basin,  
582 Southeast Spain. *J. Sed. Res., Section A: Sedimentary Petrology and Processes*, **64(2)**, 233-  
583 246.
- 584 **Hogg, A., Nasr-Azadani, M., Ungarish, M. and Meiburg, E.** (2016) Sustain gravity currents in  
585 channel. *J. Fluid Mech.*, **798**, 853-888.
- 586 **Holyer, J. Y. and Huppert, H. E.** (1980) Gravity currents entering a two- layer fluid. *J. Fluid*  
587 *Mech.*, **100(4)**, 739–767.

- 588 **Hughes, G. O.** (2016) Inside the head and tail of a turbulent gravity current. *J. Fluid Mech.*,  
589 **790**, 1–4.
- 590 **Huppert, B. H. E.** (1998) Quantitative modelling of granular suspension flows. *Philosophical*  
591 *Transactions of the Royal Society A: Mathematical, Physical and Engineering Sciences*,  
592 **356**, 2471–2496.
- 593 **Huppert, H. E.** (1982) Propagation of two-dimensional and axisymmetric viscous gravity  
594 currents over a rigid horizontal surface. *J. Fluid Mech.*, **121**, 43–58.
- 595 **Huppert, H. E.** (2006) Gravity currents: A personal perspective. *J. Fluid Mech.*, **554**, 299–322.
- 596 **Huppert, H. E.** and **Simpson, J. E.** (1980) The slumping of gravity currents. *J. Fluid Mech.*, **99(4)**,  
597 785–799.
- 598 **Islam, M. A.** and **Imran, J.** (2010) Vertical structure of continuous release saline and turbidity  
599 currents. *J. Geophys. Res.*, **115**, 1–14, doi:10.1029/2009JC005365.
- 600 **Ismail, H., Viparelli, E.** and **Imran, J.** (2016) Confluence of density currents over an erodible  
601 bed. *J. Geophys. Res.: Earth Surface*, **121**, 1251–1272.
- 602 **Jerolmack, D. J.** and **Paola, C.** (2010) Shredding of environmental signals by sediment  
603 transport. *Geophys. Res. Lett.*, **37(19)**, 1–5.
- 604 **Johnson, C. G.** and **Hogg, A. J.** (2013) Entraining gravity currents. *J. Fluid Mech.*, **731**, 477–508.
- 605 **Kneller, B.** and **Buckee, C.** (2000) The structure and fluid mechanics of turbidity currents: a  
606 review of some recent studies and their geological implications. *Sedimentology*, **47**, 62–  
607 94.
- 608 **Kneller, B.** and **McCaffrey, W. D.** (2003) The interpretation of vertical sequences in turbidite  
609 beds: the influence of longitudinal flow. *J. Sed. Res.*, **73(5)**, 706–713.
- 610 **Kneller, B. C.** and **Branney, M. J.** (1995) Sustained High-Density Turbidity Currents and the  
611 Deposition of Thick Massive Sands. *Sedimentology*, **42**, 607–616.

- 612 **Kneller, B. C., Bennett, S. J. and McCaffrey, W. D.** (1999) Velocity structure, turbulence and  
613 fluid stresses in experimental gravity currents. *J. Geophys. Res.*, **104(C3)**, 5381.
- 614 **Lowe, D.R.** (1982) Sediment gravity flows; II, Depositional models with special reference to  
615 the deposits of high-density turbidity currents. *J. Sed. Petrol.*, **52(1)**, 279-297.
- 616 **Lowe, R. J., Linden, P. F. and Rottman, J. W.** (2002) A laboratory study of the velocity structure  
617 in an intrusive gravity current. *J. Fluid Mech.*, **456**, 33–48.
- 618 **MacVicar, B. J., Dilling, S., Lacey, R. W. J. and Hipel, K.** (2014) A quality analysis of the Vectrino  
619 II instrument using a new open-source MATLAB toolbox and 2D ARMA models to detect  
620 and replace spikes. In: Schleiss AJ, de Cesare G, Franca MJ, Pfister M, (eds.), *River Flow*  
621 *2014*, CRC Press/Balkema: Leiden; 1951–1959.
- 622 **Middleton, G. V.** (1966) Experiments on density and turbidity currents II. *Can. J. Earth Sci.*, **3**,  
623 523–546.
- 624 **Middleton, G. V.** (1993) Sediment deposition from turbidity currents. *Annu. Rev. Earth Planet.*  
625 *Sci.*, **21**, 89–114.
- 626 **Mikada, H., Mitsuzawa, K., Matsumoto, H., Watanabe, T., Morita, S., Otsuka, R., Sugioka,**  
627 **H., Baba, T., Araki, E. and Suyehiro, K.** (2006) New discoveries in dynamics of an M8  
628 earthquake-phenomena and their implications from the 2003 Tokachi-oki earthquake  
629 using a long term monitoring cabled observatory. *Tectonophysics*, **426(1–2)**, 95–105.
- 630 **Mulder, T. and Alexander, J.** (2001) The physical character of subaqueous sedimentary  
631 density flow and their deposits. *Sedimentology*, **48(2)**, 269–299.
- 632 **Mulder, T. and Alexander, J.** (2001) The physical character of subaqueous sedimentary  
633 density flow and their deposits. *Sedimentology*, **48(2)**, 269–299.
- 634 **Mulder, T., Syvitski, J. P. M., Migeon, S., Faugères, J. C. and Savoye, B.** (2003) Marine  
635 hyperpycnal flows: Initiation, behavior and related deposits. A review. *Mar. Petrol. Geol.*,  
636 **20**, 861–882.

- 637 **Nakajima, T. and Kanai, Y.** (2000) Sedimentary features of seismoturbidites triggered by the  
638 1983 and older historical earthquakes in the eastern margin of the Japan Sea. *Sed. Geol.*,  
639 **135**, 1-19.
- 640 **Paola, C., Straub, K., Mohrig, D. and Reinhardt, L.** (2009) The ‘unreasonable effectiveness’ of  
641 stratigraphic and geometric experiments. *Earth-Sci. Rev.*, **97**, 1-43.
- 642 **Patton, J.R., Goldfinger, C., Morey, A.E., Ikehara, K., Romsos, C., Stoner, J., Djadjadi- hardja,**  
643 **Y., Udrek, Ardhyastuti, S., Gaffar, E.Z. and Vizcaino, A.** (2015) A 6600 year earthquake  
644 history in the region of the 2004 Sumatra-Andaman sub- duction zone earthquake.  
645 *Geosphere*, **11**, 2067–2129, doi:10.1130/GES01066.1.
- 646 **Piper, D. J. W. and Normark, W. R.** (2009) Processes That Initiate Turbidity Currents and Their  
647 Influence on Turbidites: A Marine Geology Perspective. *J. Sed. Res.*, **79**, 347–362.
- 648 **Piper, D. J. W., Cochonat, P. and Morrison, M. L.** (1999) The sequence of events around the  
649 epicentre of the 1929 GrandBanks earthquake: initiation of debris flows and turbidity  
650 current inferred from sidescan sonar. *Sedimentology*, **46**, 79–97.
- 651 **Piper, D. J. W., Shor, A. N. and Clarke, J. E. H.** (1988) The 1929 “Grand Banks” earthquake,  
652 slump, and turbidity current. *Geol. Soc. Am. Spec. Pap.*, **229**, 77–92.
- 653 **Rottman, J. W. and Simpson, J. E.** (1983) Gravity currents produced by instantaneous releases  
654 of a heavy fluid in a rectangular channel. *J. Fluid Mech.*, **135**, 95–110.
- 655 **Sequeiros, O. E.** (2012) Estimating turbidity current conditions from channel morphology: A  
656 Froude number approach. *J. Geophys. Res.: Oceans*, **117(4)**, 1–19.
- 657 **Sher, D. and Woods, A. W.** (2015) Gravity currents: entrainment, stratification and self-  
658 similarity. *J. Fluid Mech.*, **784**, 130–162.
- 659 **Shiki, T., Cita, M. and Gorsline, D.** (2000) Sedimentary features of seismites, seismo-turbidites  
660 and tsunamiites—an introduction. *Sed. Geol.*, **135**, vii–ix.



- 661 **Simpson, J. E.** (1982) Gravity currents in the laboratory, atmosphere, and ocean. *Annu. Rev.*  
662 *Fluid Mech.*, **14**, 213–234.
- 663 **Stevenson, C. J., Talling, P. J., Wynn, R. B., Masson, D. G., Hunt, J. E., Frenz, M.,**  
664 **Akhmetzhanov, A. and Cronin, B. T.** (2013) The flows that left no trace: Very large-  
665 volume turbidity currents that bypassed sediment through submarine channels without  
666 eroding the sea floor. *Mar. Petrol. Geol.*, **41**, 186–205.
- 667 **St-Onge, G., Chapron, E., Mulsow, S., Salas, M., Viel, M., Debret, M., Foucher, A., Mulder,**  
668 **T., Winiarski, T. and Desmet, M.** (2012) Comparison of earthquake-triggered turbidites  
669 from the Saguenay (Eastern Canada) and Reloncavi (Chilean margin) Fjords: implications  
670 for paleoseismicity and sedimentology. *Sed. Geol.*, **243**, 89–107.
- 671 **Sumner, E. J. and Paull, C. K.** (2014) Swept away by a turbidity current in Mendocino  
672 submarine canyon, California. *Geophys. Res. Lett.*, **41(21)**, 7611–7618.
- 673 **Sumner, E. J., Siti, M. I., McNeill, L. C., Talling, P. J., Henstock, T. J., Wynn, R. B.,**  
674 **Djajadihardja, Y. S. and Permana, H.** (2013) Can turbidites be used to reconstruct a  
675 paleoearthquake record for the central Sumatran margin? *Geology*, **41(7)**, 763–766.
- 676 **Talling, P. J.** (2013) Hybrid submarine flows comprising turbidity current and cohesive debris  
677 flow: Deposits, theoretical and experimental analyses, and generalized models.  
678 *Geosphere*, **9(3)**, 460–488.
- 679 **Talling, P. J., Allin, J., Armitage, D. A., Arnott, R. W. C., Cartigny, M. J. B., Clare, M. A., Felletti,**  
680 **F., Covault, J. A., Girardclos, S., Hansen, E., Hill, P. R., Hiscott, R. N., Hogg, A. J., Clarke,**  
681 **J. H., Jobe, Z. R., Malgesini, G., Mozzato, A., Naruse, H., Parkinson, S., Peel, F. J., Piper,**  
682 **D. J. W., Pope, E., Postma, M., Rowley, P., Sguazzini, A., Stevenson, C. J., Sumner, E. J.,**  
683 **Sylvester, Z., Watts, C. and Xu, J.** (2015) Key Future Directions for Research on Turbidity  
684 Currents and Their Deposits. *J. Sed. Res.*, **85**, 153–169.
- 685 **Xu, J. P., Noble, M. A. and Rosenfeld, L. K.** (2004) In-situ measurements of velocity structure  
686 within turbidity currents. *Geophys. Res. Lett.*, **31(9)**, 1–4.

687

688 **FIGURE CAPTIONS**

689 **Fig. 1:** Schematic sedimentary log of a turbidite with intervals of inversely graded grain size.  
690 Inverse grading in pulsed deposits is distinct from basal inverse grading, which can be  
691 produced by other mechanisms (e.g. Hand, 1997). Note: S = Silt; VF = very fine sand; F = fine  
692 sand; M = medium sand; C = coarse sand; VC = very coarse sand; G = granules. Mudstone  
693 clasts and hemipelagites are not always present.

694 **Fig. 2:** Schematic of the experimental set up. A 5 m-long flume with two lock boxes (each  
695 0.125m long) set up in series at one end to enable the delayed release of a second pulse to  
696 generate a pulsed flow. Two overflow boxes were used to reduce the effect of returning waves  
697 associated with slumping of dense fluids in the lock boxes. Acoustic-Doppler Velocimetry  
698 (ADV) was used to collect velocity data at successive downstream positions located at 0.365,  
699 0.465, 0.585, 0.675, 0.765, 0.865, 0.965, 1.065, 1.265, 1.465, 1.665 and 1.865 m.

700 **Fig. 3:** Photographs of the flow at different time intervals for (A) a single-pulsed flow  
701 experiment with 0 second delay time and (B) a multi-pulsed flow experiment with 4 second  
702 delay time between two pulses. In (B) the two pulses completed merged between 15s and  
703 18s. Gridlines on the bottom of the flume were used for camera alignment and flow position  
704 tracking. Inset shows the advection of the second pulse within the first pulse.

705 **Fig. 4:** Plots showing the location of the front of (A) a single-pulsed and (B) a multi-pulsed flow  
706 over time. Dashed curves are best fits of front position data collected from multiple  
707 experiments.

708 **Fig. 5:** Contour plots showing spatio-temporal variation of internal velocity structure within  
709 (A) a single-pulsed flow and (B) a multi-pulsed flow at 0.365 m, 0.675 m, 0.865 m, 1.265 m  
710 and 1.665 m downstream from the back of the lock box. Red and blue lines between plots  
711 indicate the arrivals of the primary and secondary pulses, respectively; these become  
712 progressively closer with time in multi-pulsed flows. Note that the low velocity variations that  
713 appear as vertical stripes of amplitude ( $< 0.025 \text{ ms}^{-1}$ ) show the effect of surface waves, white  
714 horizontal stripes in each subplot are areas of no data.

715 **Fig. 6:** Contour plots showing spatio-temporal variations of depth-averaged velocity of (A)  
716 Single-pulsed flows and (B) Multi-pulsed flows. Note: Dashed and dotted curves are best fits  
717 of front positions of primary and secondary pulses respectively.

718 **Fig. 7:** Comparison between depth-averaged velocity profiles of single- and multi-pulsed flows  
719 at three different downstream positions: (A) Raw data and (B) Filtered data. Note: Raw data  
720 were filtered by using Savitzky-Golay smoothing process in MatLab with a polynomial order  
721 of three and a framelength of 151.

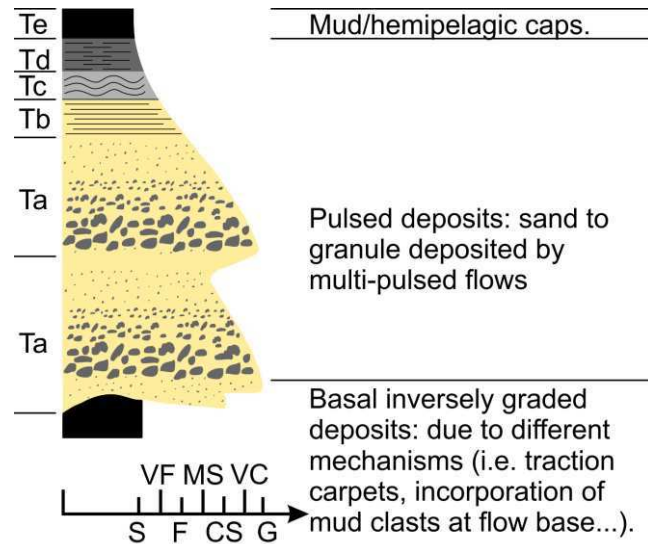
722 **Fig. 8:** Model of multi-pulsed flow propagation based on experimental results. Vertical axis  
723 shows flow height (h), horizontal axes show density (d) and velocity (v). Note: The model  
724 illustrates the scenario in which the second pulse intrudes into the first pulse at neutrally  
725 buoyant level (see text for discussion of alternative scenarios).

726 **Fig. 9:** Conceptual models illustrating the depth-averaged velocity-time profile for various  
727 turbidity current configurations and their inferred deposits. (A) A single-pulse turbidite with  
728 an upward fining grain size profile. (B) Stacked turbidites comprising two single-pulsed  
729 turbidities with a presence of Bouma Te (silt or clay layer) in between. (C) Amalgamated  
730 turbidite with sharp interface between different inverse-to-normal grading cycles due to the  
731 erosion of a latter flow into the deposit of an earlier flow. (D) Pulsed turbidites at relatively  
732 proximal and distal locations. Note: 1) the lack of linear correspondence between the time  
733 and depth records (shown schematically for Fig. 9A, and implied for 9B-D); 2) pulsed turbidites  
734 might have internal erosion surfaces instead of (or in addition to) inverse grading depending  
735 on pulse strength.

736 **Fig. 10:** Initiation mechanisms of multi-pulsed flows: **(A)** Multi-pulsed flow triggered by  
737 retrogressive slope failures and conceptual turbidite patterns for longer vs. shorter failure  
738 delays in the left-hand and right-hand panels, respectively and **(B)** Tri-pulsed flow triggered  
739 by flow combination at channels, and possible turbidite grading patterns.

740 **Fig. 11:** Multi-pulsed turbidites **(A)** offshore Sumatra at the 4MC and 2MC core locations  
741 (modified after Sumner *et al.*, 2013), dashed curve shows proposed channel conduit and **(B)**  
742 in the linked Juan de Fuca and Cascadia channels at the 12PC and 25PC locations (modified  
743 from Gutiérrez-Pastor *et al.*, 2013), white curve shows channel conduit (Goldfinger *et al.*,

744 2016). Note: because grainsize was estimated directly from the core, sediments finer than 62  
 745  $\mu\text{m}$  cannot be distinguished (A). Magnitude of magnetic data reflect grainsize of turbidites.  
 746 Bathymetric data were taken from GebCO, 2014.

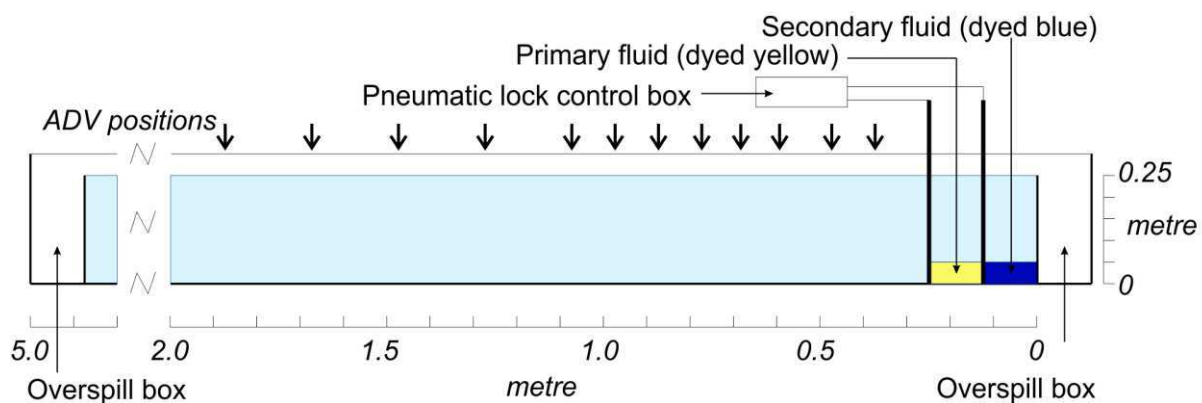


747

748 Figure 1

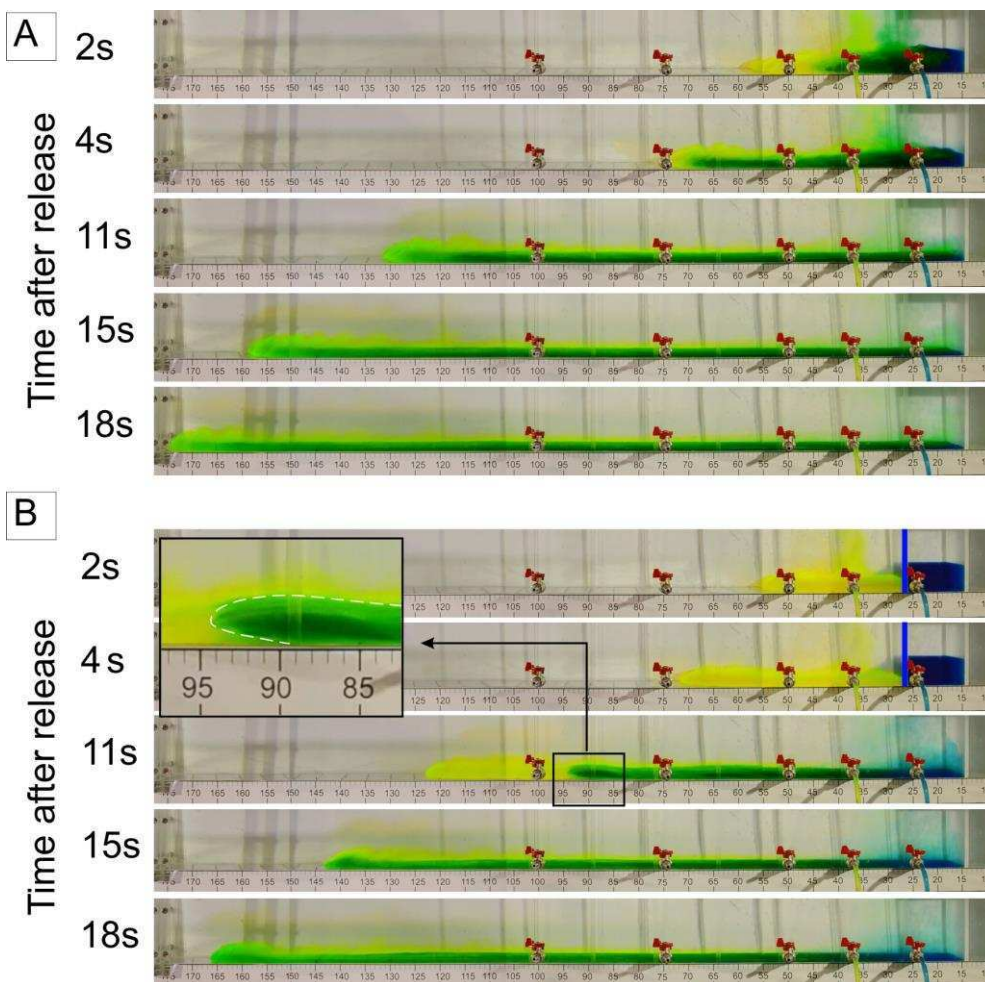
749

750



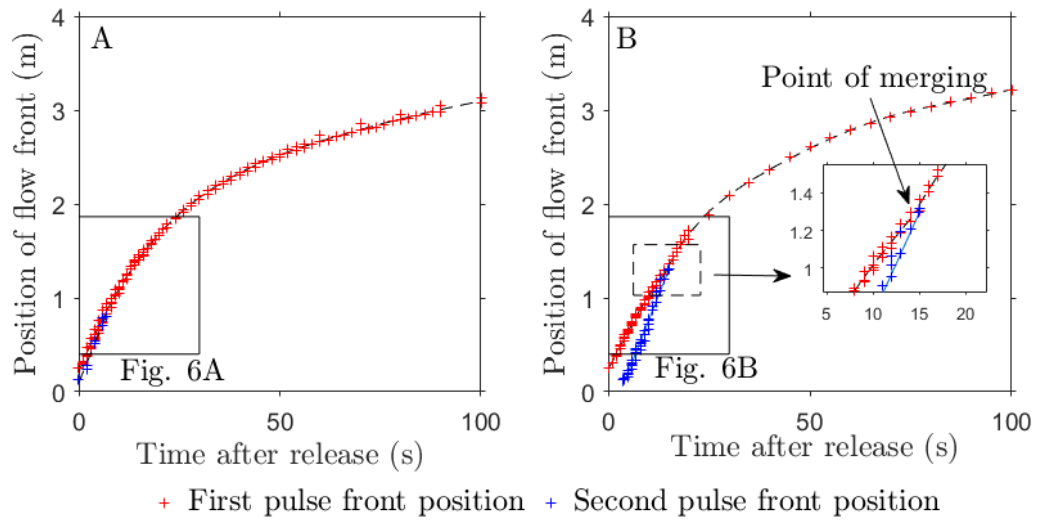
751

752 Figure 2



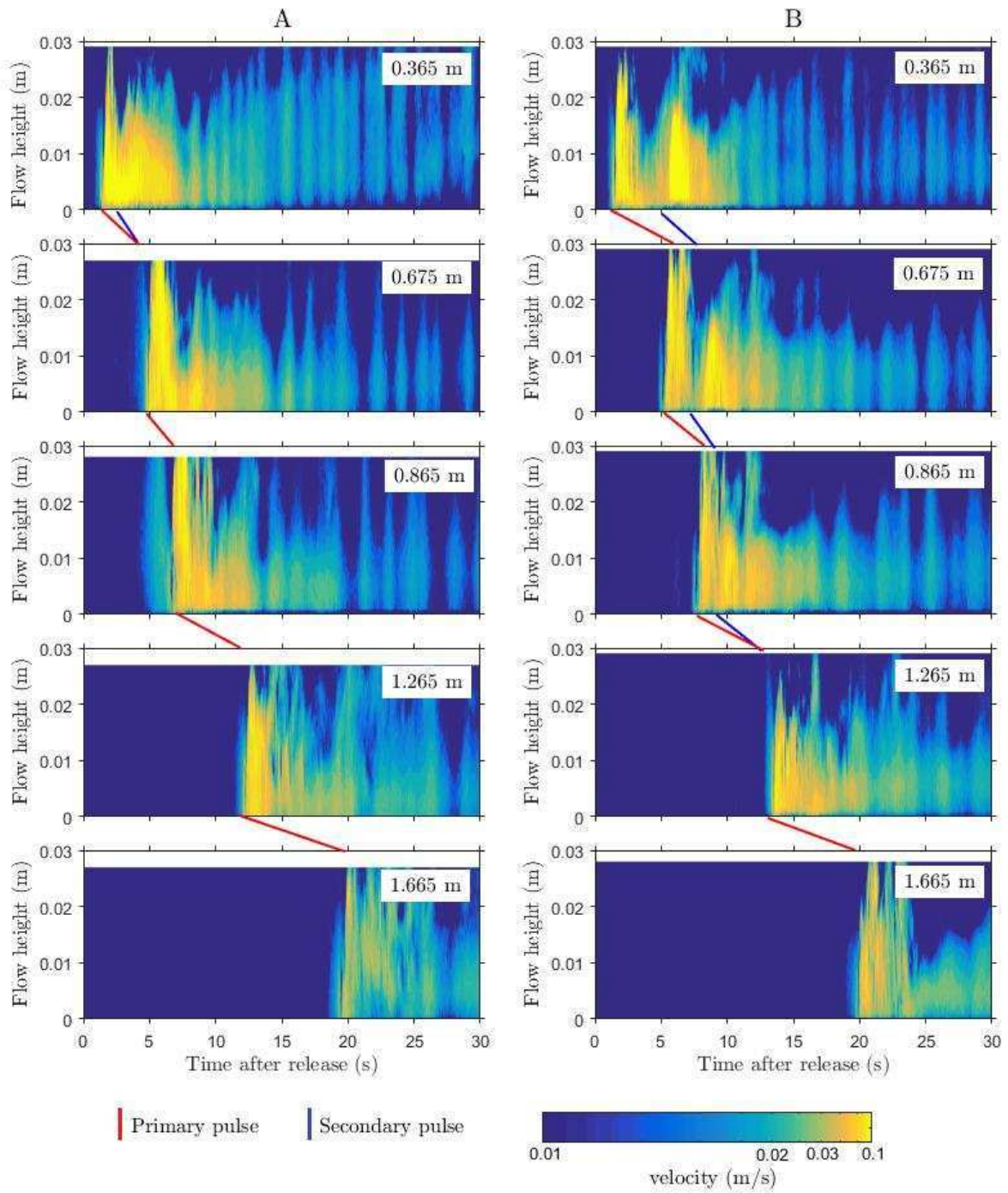
753

754 Figure 3



755

756 Figure 4

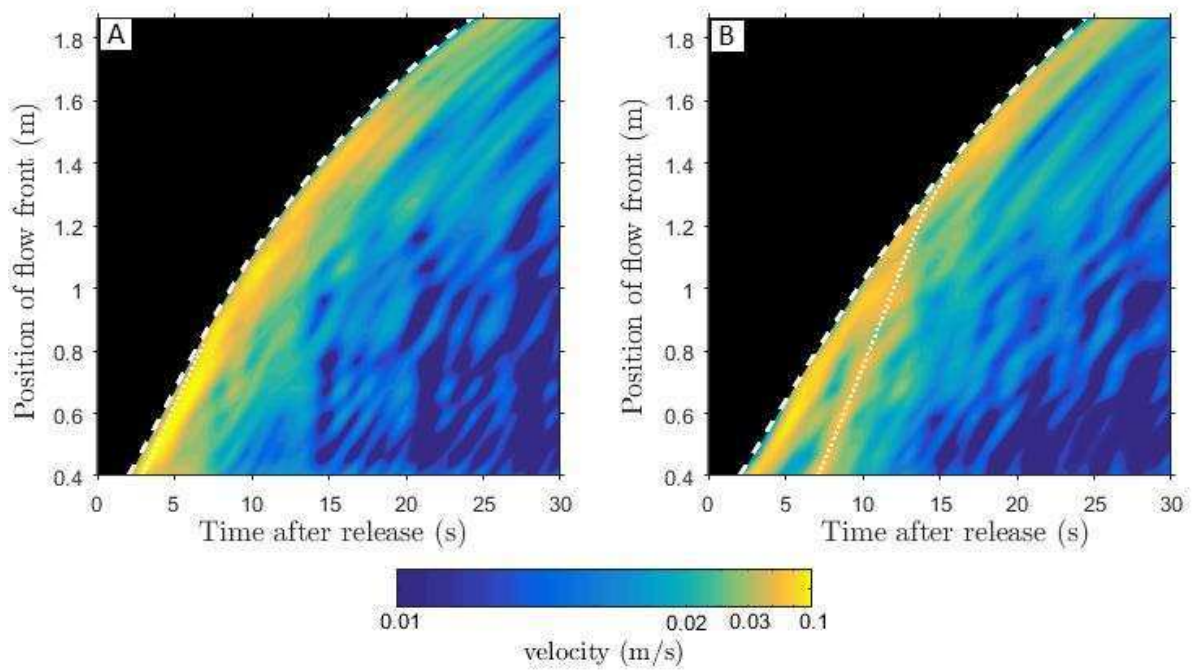


757

758 Figure 5

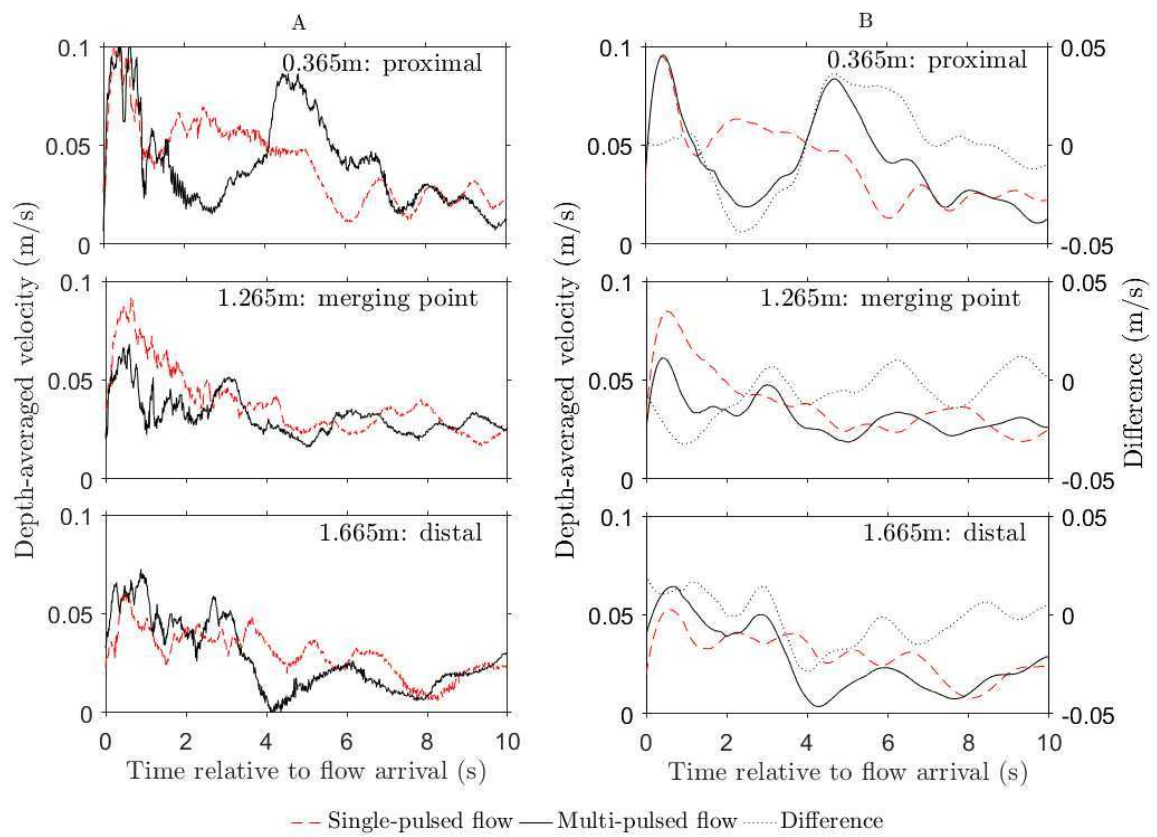
759





760

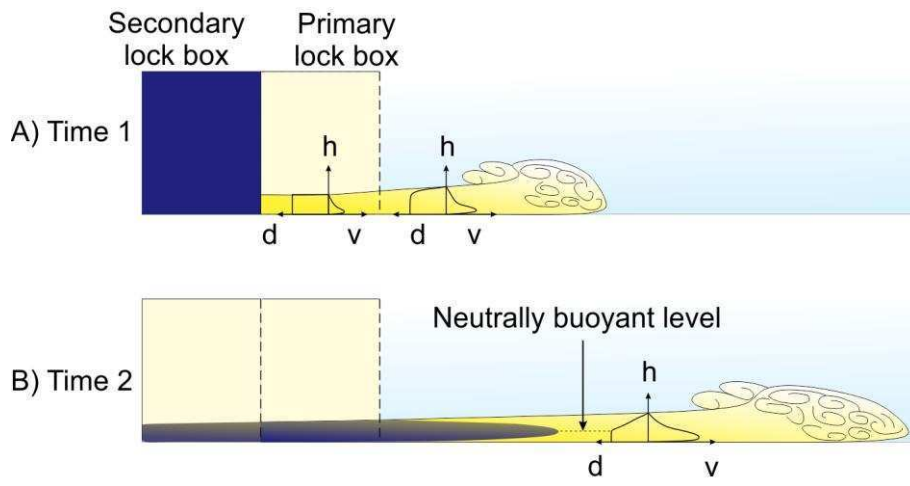
761 Figure 6



762

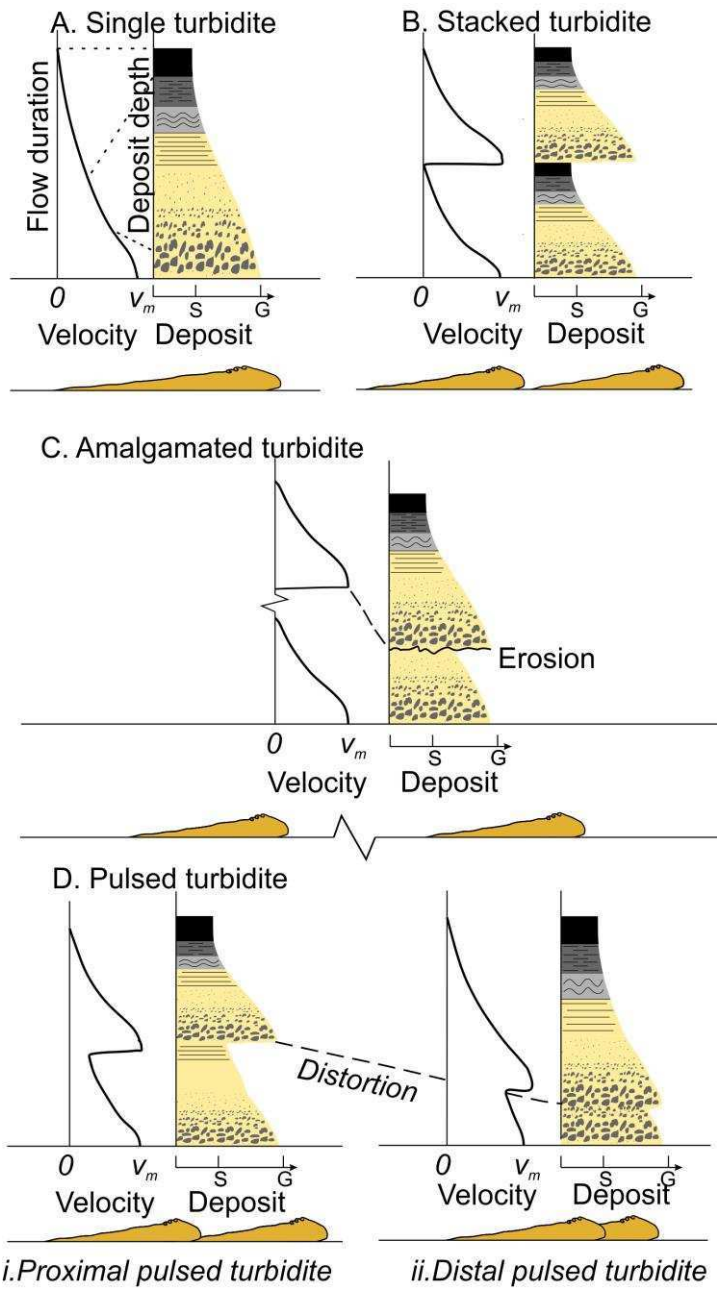
763 Figure 7





764

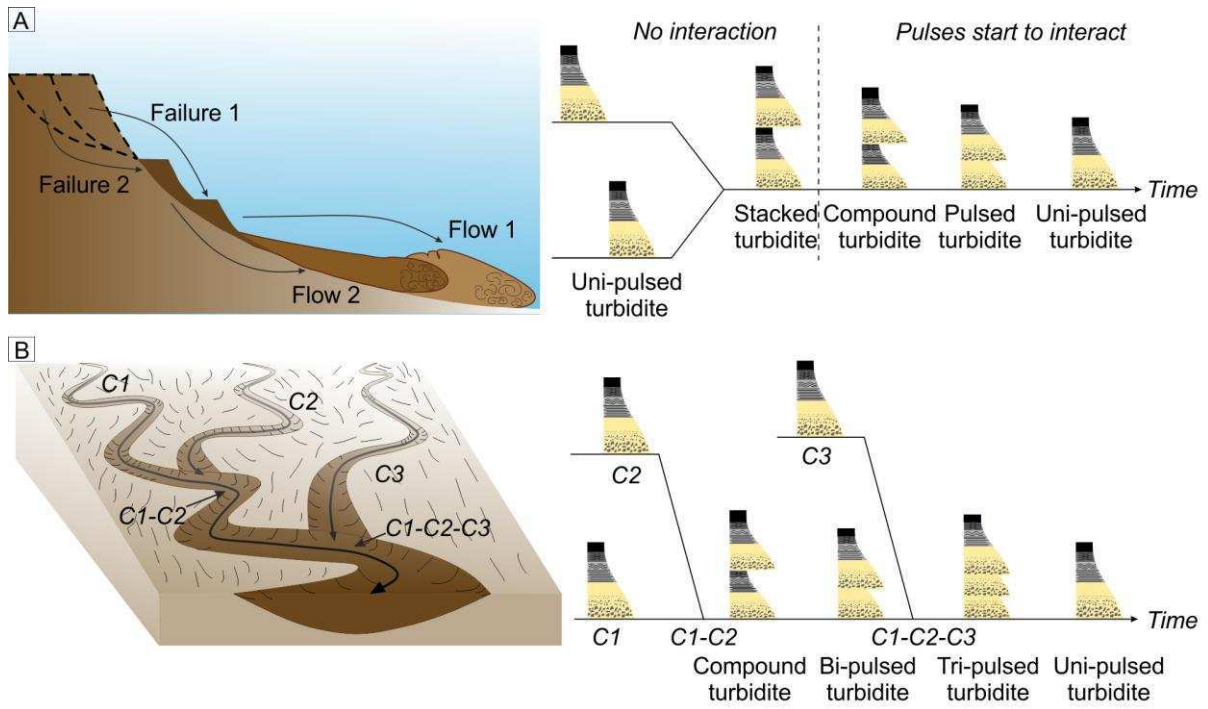
765 Figure 8



766

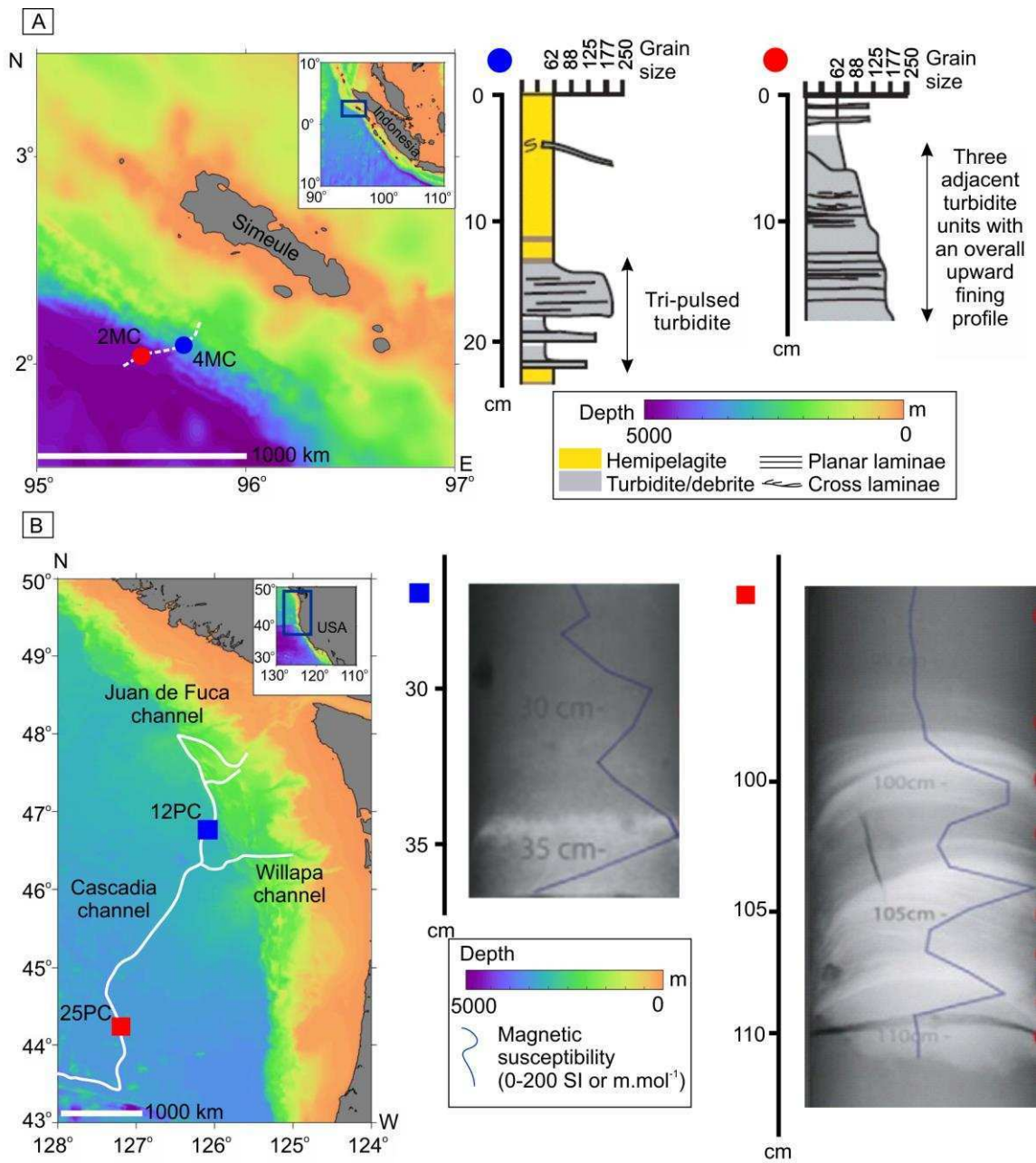
767 Figure 9

768



769

770 Figure 10



771

772 Figure 11